

Multi-Functional Polarization-Based Coverage Control through Static Passive EMSs

G. Oliveri,⁽¹⁾⁽²⁾ *Fellow, IEEE*, F. Zardi,⁽¹⁾⁽²⁾ *Member, IEEE*, A. Salas-Sanchez,⁽¹⁾⁽²⁾ *Member, IEEE*, and A. Massa,⁽¹⁾⁽²⁾⁽³⁾⁽⁴⁾⁽⁵⁾ *Fellow, IEEE*

⁽¹⁾ *ELEDIA Research Center (ELEDIA@Unitn - University of Trento)*

DICAM - Department of Civil, Environmental, and Mechanical Engineering

Via Mesiano 77, 38123 Trento - Italy

E-mail: {giacomo.oliveri, francesco.zardi, aaron.salassanchez@unitn.it, andrea.massa}@unitn.it

Website: www.eledia.org/eledia-unitn

⁽²⁾ *CNIT - "University of Trento" ELEDIA Research Unit*

Via Sommarive 9, 38123 Trento - Italy

Website: www.eledia.org/eledia-unitn

⁽³⁾ *ELEDIA Research Center (ELEDIA@UESTC - UESTC)*

School of Electronic Science and Engineering, Chengdu 611731 - China

E-mail: andrea.massa@uestc.edu.cn

Website: www.eledia.org/eledia-uestc

⁽⁴⁾ *ELEDIA Research Center (ELEDIA@TSINGHUA - Tsinghua University)*

30 Shuangqing Rd, 100084 Haidian, Beijing - China

E-mail: andrea.massa@tsinghua.edu.cn

Website: www.eledia.org/eledia-tsinghua

⁽⁵⁾ *School of Electrical Engineering*

Tel Aviv University, Tel Aviv 69978 - Israel

E-mail: andrea.massa@eng.tau.ac.il

Website: <https://engineering.tau.ac.il/>

This work has been submitted to the IEEE for possible publication. Copyright may be transferred without notice, after which this version may no longer be accessible.

Multi-Functional Polarization-Based Coverage Control through Static Passive EMSs

G. Oliveri, F. Zardi, A. Salas-Sanchez, and A. Massa

Abstract

An innovative multi-functional static-passive electromagnetic skin (*SP-EMS*) solution is proposed to simultaneously support, in reflection, two independent wave-manipulation functionalities with a single meta-atoms arrangement on the *EMS* aperture when illuminated by two *EM* sources operating at the same frequency, but working in different polarization states. Towards this end, a simple reference meta-atom is designed first to enable an accurate and independent control of each polarization component of the local reflection tensor. Successively, the macro-scale synthesis of multi-polarization (*MP*) *SP-EMS*s (*MP-SP-EMS*s) is carried out by solving a global optimization problem where a cost function, which mathematically codes separate requirements for each polarization, is minimized with a customized version of the system-by-design (*SbD*) technique. Representative results from a set of numerical and experimental tests are reported to assess the feasibility of a multi-function *EMS* based on polarization diversity as well as the effectiveness and the robustness of the proposed method for the synthesis of *MP-SP-EMS*s.

Key words: Static Passive *EM* Skins; Smart Electromagnetic Environment; Next-Generation Communications; Multi-Polarization Skins.

1 Introduction and Rationale

In the recent years, static passive electromagnetic (*EM*) skins (*SP-EMSs*) have gathered a considerable attention as a feasible technology to implement Smart Electromagnetic Environments (*SEMEs*) [1]-[3] with minimum fabrication, installation, and integration costs [4]-[8]. The macro-scale anomalous wave reflection control, enabled by the micro-scale structure of *SP-EMSs* [9][10], has been widely exploited in outdoor [5][11], indoor [4][6], and outdoor-to-indoor [12] scenarios to improve the coverage as well as to enhance the quality-of-service (*QoS*) in wireless networks. Moreover, *SP-EMSs* have been used in [7][8] as an inexpensive option to validate, in a fixed time snapshot, the performance of their reconfigurable passive counterparts (*RP-EMSs*), which are labeled as reconfigurable intelligent surfaces (*RISs*), as well.

Dealing with *SP-EMSs*, the standard *SEME* scenario generally features a single primary source, which models either a base station (outdoor case) or an access point (indoor case), that illuminates the *EMS* aperture [4][6]-[8]. Therefore, state-of-the-art design techniques have been usually conceived to support a single wave-manipulation functionality (e.g., anomalous focusing or power shaping of the reflected field) [4]-[8]. Nevertheless, any *EMS* may simultaneously support independent wave transformations for different illuminations [9][13] according to the surface electromagnetics theory. This opportunity, not yet deeply explored in *SEME* scenarios to the best of the authors' knowledge, can be of great interest in practical applications where a single *EMS* aperture, featuring multiple functionalities, could enable multiple service-providers to employ exactly the same wireless channel, while yielding independent coverage (e.g., Fig. 1).

Following this line of reasoning, this research work is devoted to assess the feasibility of multi-functional *SP-EMSs* for *SEMEs*. By leveraging the *polarization diversity* of the incident waves radiated by two different illumination sources, but operating at the same frequency (Fig. 1), a method for the synthesis of a single *EMS* panel that supports two independent wave-manipulation functionalities is introduced and applied to design multi-polarization (*MP*) *SP-EMS* (*MP-SP-EMSs*). Towards this end, a simple reference meta-atom is designed first to enable an accurate and independent control of each polarization component of the local reflection tensor. Successively, the macro-scale synthesis of multi-polarization (*MP*) *SP-EMSs*

(*MP-SP-EMSs*) is carried out by solving a global optimization problem where a cost function, which mathematically codes separate requirements for each polarization, is minimized. More specifically, a customized version of the system-by-design (*SbD*) technique is implemented to efficiently handle the huge computational burden of the large-scale problem at hand.

To the best of the authors' knowledge, the main innovative contributions of this paper include (i) the design of a low-complexity unit cell (namely, an *EMS* meta-atom) that supports an independent control on each ψ -th ($\psi \in \{TE, TM\}$) component of the reflection tensor, (ii) an *EMS* design approach to handle two simultaneous functionalities at the same frequency by exploiting the polarization diversity, and (iii) the full-wave numerical and experimental validation of the concept of multi-polarization (*MP*) *SP-EMSs* (*MP-SP-EMSs*) in different scenarios and working conditions.

The outline of the paper is as follows. After the mathematical formulation of the synthesis problem at hand, Section 2 presents the proposed method for the design of *MP-SP-EMSs* starting from a simple *EMS* meta-atom layout detailed in Sect. 3.1. Representative results from a set of numerical and experimental experiments are reported in Sect. 3.2 to assess the feasibility of a multi-function *EMS* based on polarization diversity as well as the effectiveness and the robustness of the proposed method for the synthesis of *MP-SP-EMSs*. Conclusions and final remarks follow (Sect. 4).

2 Problem Formulation and Design Process

Let us consider the multi-illumination *SEME* scenario in Fig. 1(a) where two primary sources (e.g., base stations) illuminate a *MP-SP-EMS* located on the (x, y) -plane with an incident field $\mathbf{E}^{inc}(\mathbf{r})$, \mathbf{r} ($\mathbf{r} \triangleq \sum_{c=\{x,y,z\}} c\hat{\mathbf{c}}$) being the position vector. Each source radiates a field modeled as a plane wave with a different polarization state ψ ($\psi \in \{TE, TM\}$), $\mathbf{E}_{\psi}^{inc}(\mathbf{r})$ being the associated electric field, so that

$$\mathbf{E}^{inc}(\mathbf{r}) = \mathbf{E}_{TE}^{inc}(\mathbf{r}) + \mathbf{E}_{TM}^{inc}(\mathbf{r}) = (E_{TE}^{inc}\hat{\mathbf{e}}_{TE}) \exp(-j\mathbf{k}_{TE}^{inc} \cdot \mathbf{r}) + (E_{TM}^{inc}\hat{\mathbf{e}}_{TM}) \exp(-j\mathbf{k}_{TM}^{inc} \cdot \mathbf{r}) \quad (1)$$

where

$$\mathbf{k}_\psi^{inc} = -k_0 [\sin(\theta_\psi^{inc}) \cos(\varphi_\psi^{inc}) \hat{\mathbf{x}} + \sin(\theta_\psi^{inc}) \sin(\varphi_\psi^{inc}) \hat{\mathbf{y}} + \cos(\theta_\psi^{inc}) \hat{\mathbf{z}}] \quad (2)$$

is the wave vector of the ψ -th ($\psi \in \{TE, TM\}$) incident wave component. In (1)-(2), $\hat{\mathbf{e}}_\psi$ is the ψ -th ($\psi \in \{TE, TM\}$) mode unit vector, E_ψ^{inc} is its complex-valued coefficient, and k_0 is the free-space wavenumber.

Owing to the linearity of the problem and according to the surface *EM* theory [5][9][15]-[17], the ψ -th ($\psi \in \{TE, TM\}$) polarization component of the field reflected in the far-field region by the *MP-SP-EMS*, $\mathbf{E}_\psi^{refl}(\mathbf{r}|\mathcal{D})$, is given by $\mathbf{E}_\psi^{refl}(\mathbf{r}|\mathcal{D}) \triangleq \mathbf{E}_\psi^{refl}(\theta, \varphi|\mathcal{D}) \times \frac{\exp(-jk_0 r)}{r}$ where

$$\mathbf{E}_\psi^{refl}(\theta, \varphi|\mathcal{D}) = \frac{jk_0}{4\pi} \int_{\Omega} \mathbf{J}_\psi(\mathbf{r}'|\mathcal{D}) \exp(jk_0 \hat{\mathbf{r}} \cdot \mathbf{r}') d\mathbf{r}', \quad (3)$$

$\mathbf{J}_\psi(\mathbf{r}|\mathcal{D})$ being the corresponding ψ -th ($\psi \in \{TE, TM\}$) equivalent surface current induced on the *EMS* aperture Ω (i.e., $\mathbf{r} \in \Omega$) under the ψ -th ($\psi \in \{TE, TM\}$) illumination, which is defined as follows

$$\mathbf{J}_\psi(\mathbf{r}|\mathcal{D}) \triangleq \hat{\mathbf{z}} \times [\zeta_0 \hat{\mathbf{z}} \times \mathbf{J}_\psi^e(\mathbf{r}|\mathcal{D}) + \mathbf{J}_\psi^m(\mathbf{r}|\mathcal{D})]. \quad (4)$$

Moreover, $\hat{\mathbf{r}} = \sin \theta \cos \varphi \hat{\mathbf{x}} + \sin \theta \sin \varphi \hat{\mathbf{y}} + \cos \varphi \hat{\mathbf{z}}$, ζ_0 is the free-space impedance, and \mathcal{D} is the set of *MP-SP-EMS descriptors* that univocally describes the geometrical and the physical characteristics of the $P \times Q$ meta-atoms of the *EMS*

$$\mathcal{D} \triangleq \{\underline{d}_{pq}; p = 1, \dots, P; q = 1, \dots, Q\}, \quad (5)$$

whose (p, q) -th entry ($p = 1, \dots, P; q = 1, \dots, Q$), \underline{d}_{pq} , features L descriptors (i.e., $\underline{d}_{pq} \triangleq \{d_{pq}^{(l)}; l = 1, \dots, L\}$).

By exploiting the Love's equivalence principle [5][9], the following relation between the o -th ($o \in \{e, m\}$) term of the ψ -th ($\psi \in \{TE, TM\}$) polarization component of the induced current, $\mathbf{J}_\psi^o(\mathbf{r}|\mathcal{D})$, and the *EMS* descriptors, \mathcal{D} , is deduced

$$\begin{cases} \mathbf{J}_\psi^e(\mathbf{r}|\mathcal{D}) = \frac{1}{\zeta_0} \hat{\mathbf{z}} \times \mathbf{k}_\psi^{inc} \times [\Gamma_\psi(\mathbf{r}|\mathcal{D}, \mathbf{k}_\psi^{inc}) E_\psi^{inc} \hat{\mathbf{e}}_\psi] \\ \mathbf{J}_\psi^m(\mathbf{r}|\mathcal{D}) = -\hat{\mathbf{z}} \times [\Gamma_\psi(\mathbf{r}|\mathcal{D}, \mathbf{k}_\psi^{inc}) E_\psi^{inc} \hat{\mathbf{e}}_\psi] \end{cases} \quad (6)$$

where $\Gamma_\psi(\mathbf{r}|\mathcal{D}, \mathbf{k}_\psi^{inc})$ is the ψ -th ($\psi \in \{TE, TM\}$) component of the local complex reflection tensor of the *MP-SP-EMS* layout defined by \mathcal{D} . Under the local periodicity condition [9], this

latter can be approximated as follows

$$\Gamma_{\psi}(\mathbf{r}|\mathcal{D}, \mathbf{k}_{\psi}^{inc}) \approx \sum_{p=1}^P \sum_{q=1}^Q \Gamma_{\psi}(\underline{d}_{pq}, \mathbf{k}_{\psi}^{inc}) \Pi^{pq}(\mathbf{r}), \quad (7)$$

($\psi \in \{TE, TM\}$) $\Pi_{pq}(\mathbf{r})$ being the (p, q) -th ($p = 1, \dots, P$; $q = 1, \dots, Q$) pixel basis function centered in the barycenter of pq -th meta-atom, \mathbf{r}_{pq} ($\mathbf{r}_{pq} \in \Omega$).

It is worth remarking that the relation $(\underline{d}, \mathbf{k}_{\psi}^{inc}) \leftrightarrow \Gamma_{\psi}(\underline{d}, \mathbf{k}_{\psi}^{inc})$ ($\psi \in \{TE, TM\}$) can be evaluated, depending on the layout of the reference meta-atom at hand (i.e., the L descriptors of $\underline{d} \triangleq \{d^{(l)}; l = 1, \dots, L\}$), by using either analytical, or numerical, or hybrid methods as well as artificial intelligence-based techniques [9][14][18]. In this work, a customized learning-by-example (*LBE*) AI-based strategy will be adopted as detailed afterwards. Moreover, the interested readers should notice that the previous mathematical formulation extends the framework of [5][9] to handle different impinging directions $(\theta_{\psi}^{inc}, \varphi_{\psi}^{inc})$ for each ψ -th ($\psi \in \{TE, TM\}$) incident polarization.

The problem of synthesizing a *MP-SP-EMS* that reflects two separate anomalous collimated beams under two [one for each ψ -th ($\psi \in \{TE, TM\}$) polarization] different illuminations is then stated as follows

MP-SP-EMS Design Problem - Given the incident field distributions, $\{\mathbf{E}_{\psi}^{inc}(\mathbf{r}); \psi \in \{TE, TM\}\}$, radiated on the *EMS* aperture (i.e., $\mathbf{r} \in \Omega$), by the ψ -th ($\psi \in \{TE, TM\}$) polarized primary sources, the corresponding reflection directions, $\{(\theta_{\psi}^{refl}, \varphi_{\psi}^{refl}); \psi \in \{TE, TM\}\}$, and a reference layout of the *MP* meta-atom, \underline{d} , characterized by a reflection tensor with polarization components $\{\Gamma_{\psi}(\underline{d}, \mathbf{k}_{\psi}^{inc}); \psi \in \{TE, TM\}\}$, find the optimal *MP-SP-EMS* layout (i.e., the set of descriptors, namely the degrees-of-freedom (*DoFs*) of the synthesis problem at hand, \mathcal{D}^{opt}) that minimizes the following cost function

$$\Phi(\mathcal{D}) = \sum_{\psi \in \{TE, TM\}} \alpha_{\psi} \times \left\{ \left| \mathbf{E}_{\psi}^{refl}(\theta_{\psi}^{refl}, \varphi_{\psi}^{refl} | \mathcal{D}) \right|^2 \right\}^{-1} \quad (8)$$

(i.e., $\mathcal{D}^{opt} = \arg \{\min_{\mathcal{D}} [\Phi(\mathcal{D})]\}$), α_{ψ} being the ψ -th ($\psi \in \{TE, TM\}$) user-

defined weighting parameter, while $|\mathbf{E}_\psi^{refl}| \triangleq \sqrt{\sum_{c=\{x,y,z\}} \Re^2 \left\{ \mathbf{E}_\psi^{refl} \cdot \hat{\mathbf{c}} \right\} + j \Im^2 \left\{ \mathbf{E}_\psi^{refl} \cdot \hat{\mathbf{c}} \right\}}.$

The key challenge of such an *EMS* design problem is that, unlike the standard synthesis of single anomalous reflection *EMS*s [9], here no analytical solvers, leveraging the Generalized Snell's Laws [19] and exploiting phase-conjugation, can be applied owing to the objective of simultaneously maximizing the reflection of two separate incident waves into independent directions. As a consequence, the trade-off *EMS* layout, \mathcal{D}^{opt} , turns out to be the solution of a large-scale optimization problem whose *DoFs* (i.e., the $P \times Q \times L$ entries of $\mathcal{D}^{opt} \triangleq \left\{ \left[d_{pq}^{(l)} \right]^{opt}; l = 1, \dots, L; p = 1, \dots, P; q = 1, \dots, Q \right\}$) must be adjusted to minimize the non-linear cost function (8) accounting for the *MP* working modality of the *EMS*.

Towards this end, a customized version of the iterative *SbD* strategy, discussed in [5][14], is introduced to properly address the *MP-SP-EMS Design Problem*. More specifically, the process follows the flowchart in Fig. 2 composed of the following blocks:

- **Solution Space Exploration (SSE)** - This block is aimed at optimizing the *MP-SP-EMS* descriptors by defining a succession of S iterations (s being the *SbD* iteration index, $s = 1, \dots, S$) where a set of G trial solutions, $\{\mathcal{D}_g^{(s)}; g = 1, \dots, G\}$ ($\mathcal{D}_g^{(s)} \triangleq \{d_{pq}|_g^{(s)}; p = 1, \dots, P; q = 1, \dots, Q\}$ being the g -th ($g = 1, \dots, G$) solution at the s -th ($s = 1, \dots, S$) iteration), evolves towards the global minimum, \mathcal{D}^{opt} , of the objective function (8). Because of the non-linearity of $\Phi(\mathcal{D})$, a global search mechanism based on the *Particle Swarm* paradigm [20] is used to update the set/swarm of G trial solutions at each s -th ($s = 1, \dots, S$) iteration;
- **Surface Reflection Coefficient Digital Twin (SRCDT)** - This block is devoted to infer the relation $(\underline{d}, \mathbf{k}_\psi^{inc}) \leftrightarrow \Gamma_\psi(\underline{d}, \mathbf{k}_\psi^{inc})$ for computing $\Gamma_\psi\left(\underline{d}_{pq}|_g^{(s)}, \mathbf{k}_\psi^{inc}\right)$ ($\psi \in \{TE, TM\}$) at every s -th ($s = 1, \dots, S$) *SbD* iteration for each g -th ($g = 1, \dots, G$) guess *MP* meta-atom in the (p, q) -th ($p = 1, \dots, P; q = 1, \dots, Q$) unit cell of the *EMS* aperture. Since the full-wave computation of the values of the ψ -th ($\psi \in \{TE, TM\}$) entries of the reflection tensor of the $P \times Q \times G \times S$ *MP* meta-atoms (i.e., $\{\Gamma_\psi\left(\underline{d}_{pq}|_g^{(s)}, \mathbf{k}_\psi^{inc}\right); p = 1, \dots, P; q = 1, \dots, Q; g = 1, \dots, G; s = 1, \dots, S\}$) generated within the *SbD* iterations would be computationally unfeasible, each ψ -th ($\psi \in \{TE, TM\}$) reflection function, $\Gamma_\psi(\underline{d}, \mathbf{k}_\psi^{inc})$, is approximated

with a surrogate relation $\tilde{\Gamma}_\psi(\underline{d}, \mathbf{k}_\psi^{inc})$ predicted by a *Digital Twin (DT)*⁽¹⁾ based on the statistical learning *Ordinary Kriging (OK)* method [5][14][18][21] and trained with a set of N known pairs/examples, $\{[\underline{d}, \mathbf{k}_\psi^{inc}]_n, \Gamma_\psi([\underline{d}, \mathbf{k}_\psi^{inc}]_n) \mid \psi \in \{TE, TM\}; n = 1, \dots, N\}$;

- **Surface-Current Evaluation (SCE)** - For each g -th ($g = 1, \dots, G$) trial *EMS* layout at the s -th ($s = 1, \dots, S$) *SbD* iteration, $\mathcal{D}_g^{(s)}$, this block implements (6) to determine the o -th ($o \in \{e, m\}$) term of the ψ -th ($\psi \in \{TE, TM\}$) polarization component of the induced current, $\mathbf{J}_\psi^o(\mathbf{r}|\mathcal{D})$, starting from the knowledge of the ψ -th ($\psi \in \{TE, TM\}$) incident field, $\mathbf{E}_\psi^{inc}(\mathbf{r})$, and the corresponding reflection coefficient, $\Gamma_\psi(\mathbf{r}|\mathcal{D}_g^{(s)}, \mathbf{k}_\psi^{inc})$, through (7) by inputting the $P \times Q$ values of $\{\Gamma_\psi(\underline{d}_{pq}|_g^{(s)}, \mathbf{k}_\psi^{inc}); p = 1, \dots, P; q = 1, \dots, Q\}$ predicted in the *SRCDT* block;
- **Far Field Computation (FFC)** - This block computes $\mathbf{E}_\psi^{refl}(\theta, \varphi|\mathcal{D}_g^{(s)})$ ($\psi \in \{TE, TM\}$) by first substituting in (4) the ψ -th ($\psi \in \{TE, TM\}$) currents, $\{\mathbf{J}_\psi^o(\mathbf{r}|\mathcal{D}_g^{(s)}); o \in \{e, m\}\}$ determined in the *SCE* block and finally inputting the result in (3);
- **Cost Function Evaluation (CFE)** - This block implements (8) to compute the cost function value of the g -th ($g = 1, \dots, G$) trial *EMS* layout guessed at the s -th ($s = 1, \dots, S$) *SbD* iteration, $\Phi(\mathcal{D}_g^{(s)})$, from the value of $\mathbf{E}_\psi^{refl}(\theta, \varphi|\mathcal{D}_g^{(s)})$ ($\psi \in \{TE, TM\}$) computed in the *FFC* block.

3 Numerical and Experimental Validation

The objective of this section is twofold. In Sect. 3.1, the design of a low-complexity *MP* meta-atom suitable for the implementation of a *MP-SP-EMS* structure is assessed. Otherwise, Section 3.2 is devoted to analyze the wave manipulation performance of a set of multi-functional *EMS* layouts yielded by properly arranging, on the *EMS* aperture and according to the synthesis method detailed in Sect. 2, suitable parametric-variations of the reference meta-atom of Sect.

⁽¹⁾It is worth noticing that in this case, unlike [5][14] where the generalized sheet transition condition technique has been adopted, the *DT* predicts the local reflection coefficients as a function of both the unit-cell geometry, \underline{d} , and the incidence-wave directions, $\{\mathbf{k}_\psi^{inc}; \psi \in \{TE, TM\}\}$, which here are different ($\mathbf{k}_{TE}^{inc} \neq \mathbf{k}_{TM}^{inc}$).

3.1. Towards this end, the analytic predictions of the behavior of the synthesized *EMS*s are compared with full-wave numerical simulations performed in *Ansys HFSS* [22] and experimental measurements (Sect. 3.2).

In the following, the primary sources have been assumed to operate at $f_0 = 28$ [GHz] and to illuminate the *EMS* panel with unitary fields (i.e., $E_\psi^{inc} = 1$ [V/m], $\psi \in \{TE, TM\}$) by setting $\varphi_\psi^{inc} = \varphi_\psi^{refl} = 0$ [deg] ($\psi \in \{TE, TM\}$), as well. As for the manufacturing of the *EMS* meta-atom and the arising *MP-SP-EMS*s, a $H = 5.1 \times 10^{-4}$ [m]-thick Rogers *RO3003* sheet with dielectric relative permittivity and dielectric loss tangent equal to $\varepsilon_r = 3.0$ and $\tan \delta = 1.0 \times 10^{-3}$, respectively, has been chosen for the *EMS* substrate, while all the metallizations of the *EMS* layout have been realized with a standard copper layer of thickness 35 [μ m].

3.1 Meta-Atom Design

To prove the feasibility of the *MP-SP-EMS* concept, a unit cell geometry (i.e., \underline{d}) supporting an *independent* control on each ψ -th ($\psi \in \{TE, TM\}$) polarization-component of the reflection tensor, $\Gamma_\psi(\underline{d}, \mathbf{k}_\psi^{inc})$, with a minimum topological complexity (e.g., $L \downarrow$) is needed. However, state-of-the-art *EMS* atoms, based on square metallizations on single-layer substrates, are not suitable because of their single polarization features [5][6][8]. On the other hand, advanced patterning layouts as in [4] were not adopted since too complex and expensive for a cheap and accessible prototyping especially in view of (future) wide deployments. Starting from these considerations, the meta-atom sketched in Fig. 1(b), which consists of a single rectangular patch printed on a single-layer substrate and is characterized by $L = 2$ *DoFs*, has been selected. To evaluate the achievable magnitude/phase control on each ψ -th ($\psi \in \{TE, TM\}$) reflected field component, such an *EMS* unit-cell has been numerically modeled in *Ansys HFSS* when replicated in each sub-domain of a square lattice with periodicity $\Delta x = \Delta y = 0.4\lambda$ by setting periodic boundary conditions under the local periodicity approximation.

Figure 3 gives the ψ -th ($\psi \in \{TE, TM\}$) reflection coefficient, $\Gamma_\psi(\underline{d}, \mathbf{k}_\psi^{inc})$, as a function of the L descriptors of the meta-atom (i.e., $d^{(1)}$ and $d^{(2)} \rightarrow L = 2$) when this latter is illuminated from broadside by the two co-located primary sources [i.e., $\theta_\psi^{inc} = 0$ [deg] ($\psi \in \{TE, TM\}$)]. Regardless of the ψ -th ($\psi \in \{TE, TM\}$) polarization of the source and the topological vari-

ations of the atom [i.e., geometrical variations of each l -th ($l = 1, \dots, L$) descriptor, $d^{(l)}$], the reflection efficiency is always greater than 90 % (98 % in a wide part of the range of variation of the $L = 2$ variables), the magnitude of any ψ -th ($\psi \in \{TE, TM\}$) reflection coefficient being always greater than -0.5 [dB] (i.e., $|\Gamma_\psi(\underline{d}, \mathbf{k}_\psi^{inc})| > -0.5$ [dB]) and generally close to -0.1 [dB] [Fig. 3(a) and Fig. 3(c)]. Moreover, the value of the phase coverage index, $\Delta\Gamma_\psi(\mathbf{k}_\psi^{inc})$ ($\Delta\Gamma_\psi(\mathbf{k}_\psi^{inc}) \triangleq \max_{\underline{d}} [\angle\Gamma_\psi(\underline{d}, \mathbf{k}_\psi^{inc})] - \min_{\underline{d}} [\angle\Gamma_\psi(\underline{d}, \mathbf{k}_\psi^{inc})]$), for both polarization components ($\psi \in \{TE, TM\}$) turns out to be close to the full 360 [deg] range (i.e., $\Delta\Gamma_\psi(\mathbf{k}_\psi^{inc}) \approx 325$ [deg], $\psi \in \{TE, TM\}$) since almost all the phase values of the reflection coefficients between -180 [deg] and 180 [deg] can be yielded by an available/admissible setup of the atom variables, $\{d^{(l)}; l = 1, \dots, L\}$ [Fig. 3(b) and Fig. 3(d)].

These outcomes prove that the unit-cell model in Fig. 1(b) fulfils the conditions for yielding anomalous wave-manipulation properties with minimum phase-quantization distortions. Finally, it is also worth mentioning that, as expected from the theoretical viewpoint, both the magnitude and the phase response of such meta-atom exhibit a polarization symmetry (i.e., $|\Gamma_{TE}(d_1, d_2; \mathbf{k}_{TE}^{inc})| = |\Gamma_{TM}(d_2, d_1; \mathbf{k}_{TE}^{inc})|$ [Fig. 3(a) and Fig. 3(c)] and $\angle\Gamma_{TE}(d_1, d_2; \mathbf{k}_{TE}^{inc}) = \angle\Gamma_{TM}(d_2, d_1; \mathbf{k}_{TE}^{inc})$ [Fig. 3(b) and Fig. 3(d)] owing to the rotational symmetry of its layout [Fig. 1(b)].

3.2 EMS Design and Validation

Starting from the meta-atom described in Sect. 3.1, the design process of *MP-SP-EMS*s has been carried out by setting $\alpha_\psi = 1.0$ ($\psi \in \{TE, TM\}$) and choosing the values of the calibration parameters of the *SbD*-based optimization according to the guidelines in [5], namely $S = 10^4$ and $G = 10^2$.

The synthesis of a square $P \times Q = 20 \times 20$ *EMS* of side $\mathcal{L} \approx 8.57 \times 10^{-2}$ has been addressed first (*Test Case 1*) by co-locating the pair of primary sources so that $\theta_\psi^{inc} = 0$ [deg] ($\psi \in \{TE, TM\}$) and requiring anomalous reflections towards $\theta_{TE}^{refl} = 30$ [deg] and $\theta_{TM}^{refl} = -40$ [deg], respectively. The sketch of the *HFSS* model derived from the descriptors, \mathcal{D}^{opt} , of the synthesized *MP-SP-EMS* is reported in Fig. 4. As expected, the arising arrangement of the *EMS* meta-atoms is characterized by a non-uniform distribution of irregular rectangular shapes

(Fig. 4). Indeed, it is the trade-off result for yielding two co-existing target functionalities, each one requiring a different distribution, on the same *EMS* aperture, of the phase of the local reflection coefficient (i.e., $\angle\Gamma_{TE}(\mathbf{r}|\mathcal{D}, \mathbf{k}_{TE}^{inc})$ [Fig. 5(a)] and $\angle\Gamma_{TM}(\mathbf{r}|\mathcal{D}, \mathbf{k}_{TM}^{inc})$ [Fig. 5(b)]). The analytically-simulated fields reflected by such an *EMS* are shown in Figs. 5(c)-5(d) by using the (u, v) direction cosines representation ($u \triangleq \sin \theta \cos \varphi$, $v \triangleq \sin \theta \sin \varphi$). More in detail, each ψ -th ($\psi \in \{TE, TM\}$) pattern has been computed separately for the two co-located illuminations by setting either $(E_{TE}^{inc} = 1, E_{TM}^{inc} = 0)$ [Fig. 5(c)] or $(E_{TE}^{inc} = 0, E_{TM}^{inc} = 1)$ [Fig. 5(d)]. As it can be observed, the *MP-SP-EMS* implements a well controlled anomalous reflection along $\theta_{TE}^{refl} = 30$ [deg] [$\rightarrow (u, v) = (0.5, 0.0)$ - Fig. 5(c)] as well as towards $\theta_{TM}^{refl} = -40$ [deg] [$\rightarrow (u, v) = (-0.64, 0.0)$ - Fig. 5(d)] when illuminated by the *TE*- or the *TM*-source, respectively. Moreover, despite the elementary layout of the meta-atom in Fig. 1(b), the synthesized *EMS* reflects a field pattern with well-controlled secondary lobes, not only along the $\varphi = 0$ cut (Fig. 6), but in the whole visible range Θ ($\Theta \triangleq \{(u, v) | u^2 + v^2 = 1\}$) [Figs. 5(c)-5(d)]. Furthermore, the faithful matching between analytical predictions and full-wave *Ansys HFSS* simulations (Fig. 6) demonstrates the reliability of the local periodicity approximation (see Sect. 2) as well as the marginal impact of both the (non-uniform) mutual coupling among the *EMS* meta-atoms and the edge truncation effects of the finite-size *EMS* aperture. These results assess the feasibility of a multi-functional *EMS* that offers a separate response for each of the two independent incident fields thanks to the polarization diversity mechanism.

In the second experiment of the first test case, the direction of incidence on the *EMS* panel of the impinging wave has been varied from broadside [$\theta_{\psi}^{inc} = 0$ [deg] ($\psi \in \{TE, TM\}$)] to $\theta_{\psi}^{inc} = -30$ [deg] ($\psi \in \{TE, TM\}$), while keeping unaltered the reflection directions to $\theta_{TE}^{refl} = 30$ [deg] and $\theta_{TM}^{refl} = -40$ [deg]. The $P \times Q$ atoms layout of the synthesized *EMS* is shown in Fig. 7(a), while the plots of both analytically-computed and full-wave simulated reflected field patterns in the $\varphi = 0$ [deg] plane are given in Fig. 7(b) to assess the flexibility/generalizability of the proposed technological solution in achieving the desired multi-functional properties for different incidence directions [i.e., $\theta_{\psi}^{inc} \neq (0, 0)$ [deg], $\psi \in \{TE, TM\}$].

The scalability of the proposed design concept to wider arrangements is evaluated next (*Test Case 2*), but maintaining the same incidence/reflection conditions of Fig. 7. By considering

two different *EMS* apertures composed of $P \times Q = 30 \times 30$ ($\rightarrow \mathcal{L} \approx 1.28 \times 10^{-1}$ [m]) and $P \times Q = 40 \times 40$ ($\rightarrow \mathcal{L} \approx 1.71 \times 10^{-2}$ [m]) unit-cells, the optimized *EMS* layouts in Fig. 8 have been obtained. Regardless of the *EMS* size, a reliable polarization-based coverage control with well controlled sidelobes is implemented as highlighted in Fig. 9(a) ($P \times Q = 30 \times 30$) and Fig. 9(b) ($P \times Q = 40 \times 40$) where the reflection patterns in the $\varphi = 0$ [deg] cut are reported. Concerning the computational load of the *EMS* synthesis, even though the *CPU*-time grows linearly with the number of meta-atoms of the *EMS*, the optimization process detailed in Sect. 2 turns out to be very efficient and competitive to handle standard *EMS* apertures. For instance, the design of a $P \times Q = 20 \times 20$ elements *EMS* requires⁽²⁾ less than 50 [sec] (i.e., $\Delta t|_{P \times Q=20 \times 20} \approx 4.1 \times 10^1$ [sec]), while the synthesis of a wider *EMS* of size $P \times Q = 40 \times 40$ needs less than 3 [min] (i.e., $\Delta t|_{P \times Q=40 \times 40} \approx 1.7 \times 10^2$ [sec]).

The final representative example (*Test Case 3*) considers separated (i.e., $\theta_{TE}^{inc} \neq \theta_{TM}^{inc}$) primary sources. More specifically, the $P \times Q = 40 \times 40$ ($\rightarrow \mathcal{L} \approx 1.71 \times 10^{-2}$ [m]) *EMS* in Fig. 10(a) has been designed subject to the following set of constraints: $\theta_{TE}^{inc} = -30$ [deg], $\theta_{TM}^{inc} = 40$ [deg], $\theta_{TE}^{refl} = 20$ [deg], and $\theta_{TM}^{refl} = -20$ [deg] [$\varphi_{\psi}^{inc} = \varphi_{\psi}^{refl} = 0.0$ ($\psi \in \{TE, TM\}$)]. Moreover, a prototype of the synthesized *EMS* layout has been built (Fig. 10) to also experimentally assess the effectiveness of *MP-SP-EMS*s as well as to evaluate the impact of the fabrication tolerances on the reflection performance of the *EMS*. In particular, the arising arrangement of meta-atoms has been manufactured on a $H = 5.1 \times 10^{-4}$ [m]-thick Rogers *RO3003* with a standard *PCB* prototyping methodology [Fig. 10(b)]. The measurement process has been performed in a semi-anechoic chamber by using a *RF* source operating at $f_0 = 28$ [GHz] and a standard horn antenna with 15 [dB] gain has been used for both the primary source and the *EM* field probe. The transmitting antenna has been installed on a fixed support located ≈ 100 [cm] away from the *MP-SP-EMS*, while both the *EMS* and the illuminator have been located on a mechanically rotating platform to automatically collect the reflected pattern samples in the whole azimuth plane (Fig. 11). The reflected field values of each ψ -th ($\psi \in \{TE, TM\}$) polarization have been measured in different and subsequent sessions by suitably rotating the horn antennas.

Figure 11 shows an excellent agreement among analytically-simulated, numerically-computed,

⁽²⁾The simulation time is related to an execution of a non-optimized MATLAB serial implementation of the synthesis algorithm on a standard laptop with a single-core 1.6 GHz CPU.

and measured (normalized to the transmitting/receiving antenna gain) reflection patterns. Such an outcome confirms, also experimentally, the possibility to implement independent functionalities with a single *SP-EMS* that serves two (also separated) orthogonally-polarized primary sources. Moreover, it is worth pointing out that the *EMS* performance/functionalities turn out marginally affected by the unavoidable fabrication tolerances (Fig. 11) thanks to the intrinsic robustness and the simplicity of the *EMS* meta-atom in Fig. 1(b).

4 Conclusions and Final Remarks

The concept of multi-functional *SP-EMS*s for *SEME*s has been demonstrated by yielding an independent control of the reflection of two incident fields at the same frequency with orthogonal polarizations. The design of the micro-scale features of the *EMS*, which is requested to simultaneously support two macro-scale functionalities in reflection, has been recast as a global optimization problem then solved with a customized *SbD*-based approach.

From the numerical and experimental assessment, the following main outcomes can be drawn:

- it is possible to design a *MP-SP-EMS* that enables an independent control of the anomalous reflection of the waves radiated towards the *EMS* panel by two differently-polarized sources working at the same frequency [e.g., Figs. 5(c)-5(d), Fig. 7(b), Fig. 9, and Fig. 11];
- the physical implementation of a *MP-SP-EMS* requires neither complex meta-atom layouts nor expensive (e.g., multi-layers) substrates as confirmed by the manufactured prototype (Fig. 10);
- the proposed design process (Sect. 2) turns out to be effective (faithfully fulfilling the design constraints), reliable (the analytic predictions adequately matching both numerical simulations and experimental measurements), and numerically efficient (the *CPU*-time being affordable in handling standard - even large - apertures for *SEME*s).

Future works, beyond the scope of the current manuscript, will be aimed at (i) generalizing the proposed multi-functional working principle to *RP-EMS*s and (ii) exploiting the available

functionalities to enable integrated sensing and communication (ISAC) services.

Acknowledgements

This work benefited from the networking activities carried out within the Project ICSC National Centre for HPC, Big Data and Quantum Computing (CN HPC) funded by the European Union - NextGenerationEU within the PNRR Program (CUP: E63C22000970007), the Project DICAM-EXC funded by the Italian Ministry of Education, Universities and Research (MUR) (Departments of Excellence 2023-2027, grant L232/2016), the Project INSIDE-NEXT - Indoor Smart Illuminator for Device Energization and Next-Generation Communications funded by the Italian Ministry for Universities and Research within the PRIN 2022 Program (CUP: E53D23000990001), and the Project AURORA - Smart Materials for Ubiquitous Energy Harvesting, Storage, and Delivery in Next Generation Sustainable Environments funded by the Italian Ministry for Universities and Research within the PRIN-PNRR 2022 Program, and the Project Partnership on Telecommunications of the Future (PE000000001 - program RESTART), funded by the European Union under the Italian National Recovery and Resilience Plan (NRRP) of NextGenerationEU (CUP: E63C22002040007). A. Massa wishes to thank E. Vico and L. Massa for the never-ending inspiration, support, guidance, and help.

References

- [1] F. Yang, D. Erricolo, and A. Massa, “Guest Editorial - Smart Electromagnetic Environment,” *IEEE Trans. Antennas Propag.*, vol. 70, no. 10, pp. 8687-8690, Oct. 2022.
- [2] A. Massa, A. Benoni, P. Da Ru, S. K. Goudos, B. Li, G. Oliveri, A. Polo, P. Rocca, and M. Salucci, “Designing smart electromagnetic environments for next-generation wireless communications,” *Telecom*, vol. 2, no. 2, pp. 213-221, 2021.
- [3] M. Barbuto, Z. Hamzavi-Zarghani, M. Longhi, A. Monti, D. Ramaccia, S. Vellucci, A. Toscano, and F. Bilotti, “Metasurfaces 3.0: a New paradigm for enabling smart electro-

- magnetic environments,” *IEEE Trans. Antennas Propag.*, vol. 70, no. 10, pp. 8883-8897, Oct. 2022.
- [4] A. F. Vaquero, E. Martinez-de-Rioja, M. Arrebola, J. A. Encinar and M. Achour, “Smart electromagnetic skin to enhance near-field coverage in mm-Wave 5G indoor scenarios,” *IEEE Trans. Antennas Propag.*, vol. 72, no. 5, pp. 4311-4326, May 2024.
- [5] G. Oliveri, P. Rocca, M. Salucci, and A. Massa, “Holographic smart EM skins for advanced beam power shaping in next generation wireless environments,” *IEEE J. Multiscale Multiphys. Comput. Techn.*, vol. 6, pp. 171-182, Oct. 2021.
- [6] A. Benoni, F. Capra, M. Salucci, and A. Massa, “Toward real-world indoor smart electromagnetic environments - A large-scale experimental demonstration,” *IEEE Trans. Antennas Propag.*, vol. 71, no. 11, pp. 8450-8463, Nov. 2023.
- [7] D. An, S. Chang, M. Hwang, Y. Youn, D. Kim, C. Lee, and W. Hong, “Diagnosis and modification of propagating electromagnetic waves using DoA systems and EM skins,” *IEEE Trans. Antennas Propag.*, vol. 72, no. 4, pp. 3629-3640, Apr. 2024.
- [8] Y. Liu, Z. Liu, S. V. Hum, and C. D. Sarris, “An equivalence principle-based hybrid method for propagation modeling in radio environments with reconfigurable intelligent surfaces,” *IEEE Trans. Antennas Propag.*, vol. 72, no. 7, pp. 5961-5973, Jul. 2024.
- [9] F. Yang and Y. Rahmat-Samii, *Surface Electromagnetics with Applications in Antenna, Microwave, and Optical Engineering*. Cambridge, UK: Cambridge University Press, 2019.
- [10] A. Alu, N. Engheta, A. Massa, and G. Oliveri, Eds., *Metamaterials-by-Design: Theory, Technologies, and Vision*. Amsterdam, NL: Elsevier, 2024.
- [11] G. Oliveri, M. Salucci, and A. Massa, “Features and potentialities of static passive EM skins for NLOS specular wireless links,” *IEEE Trans. Antennas Propag.*, vol. 71, no. 10, pp. 8048-8060, Oct. 2023.

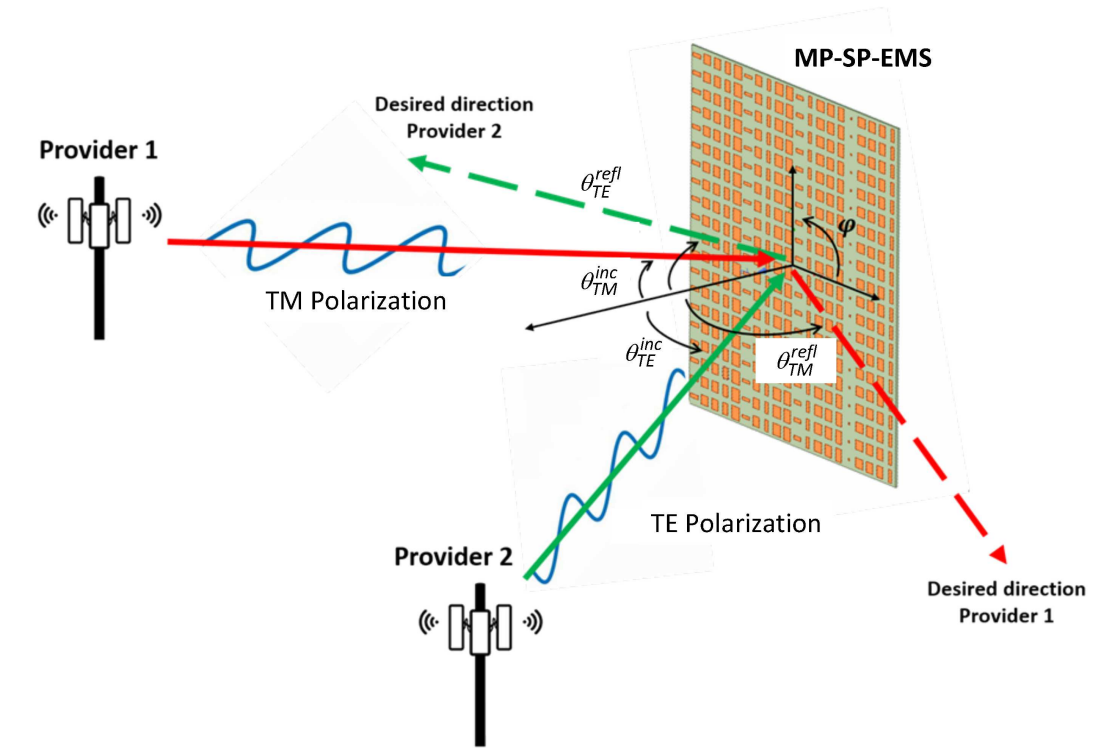
- [12] G. Oliveri, F. Zardi, G. Gottardi, and A. Massa, "Optically-transparent EM skins for Outdoor-to-Indoor mm-Wave wireless communications," *IEEE Access*, vol. 12, pp. 65178-65191, 2024.
- [13] K. Achouri, M. A. Salem, and C. Caloz, "General metasurface synthesis based on susceptibility tensors," *IEEE Trans. Antennas Propag.*, vol. 63, no. 7, pp. 2977-2991, Jul. 2015.
- [14] G. Oliveri, F. Zardi, P. Rocca, M. Salucci, and A. Massa, "Building a smart EM environment - AI-enhanced aperiodic micro-scale design of passive EM skins," *IEEE Trans. Antennas Propag.*, vol. 70, no. 10, pp. 8757-8770, Oct. 2022.
- [15] G. Oliveri, M. Salucci, and A. Massa, "Generalized analysis and unified design of EM skins," *IEEE Trans. Antennas Propag.*, vol. 71, no. 8, pp. 6579-6592, Aug. 2023.
- [16] I. V. Lindell and A. Sihvola, *Boundary Conditions in Electromagnetics*. IEEE Press, 2019.
- [17] A. Osipov and S. Tretyakov, *Modern electromagnetic scattering theory with applications*. John Wiley & Sons, 2017.
- [18] M. Salucci, L. Tenuti, G. Oliveri, and A. Massa, "Efficient prediction of the EM response of reflectarray antenna elements by an advanced statistical learning method," *IEEE Trans. Antennas Propag.*, vol. 66, no. 8, pp. 3995-4007, Aug. 2018.
- [19] N. Yu, P. Genevet, M. A. Kats, F. Aieta, J. P. Tetienne, F. Capasso, and Z. Gaburro, "Light propagation with phase discontinuities: generalized laws of reflection and refraction," *Science*, vol. 334, no. 6054, pp. 333-337, Oct. 2011.
- [20] P. Rocca, M. Benedetti, M. Donelli, D. Franceschini, and A. Massa, "Evolutionary optimization as applied to inverse problems," *Inv. Probl.*, vol. 25, art no. 123003, pp. 1-41, Dec. 2009.
- [21] G. Oliveri, M. Salucci, and A. Massa, "Towards efficient reflectarray digital twins - An EM-driven machine learning perspective," *IEEE Trans. Antennas Propag.*, vol. 70, no. 7, pp. 5078-5093, Jul. 2022.
- [22] ANSYS Electromagnetics Suite - HFSS (2021). ANSYS, Inc.

FIGURE CAPTIONS

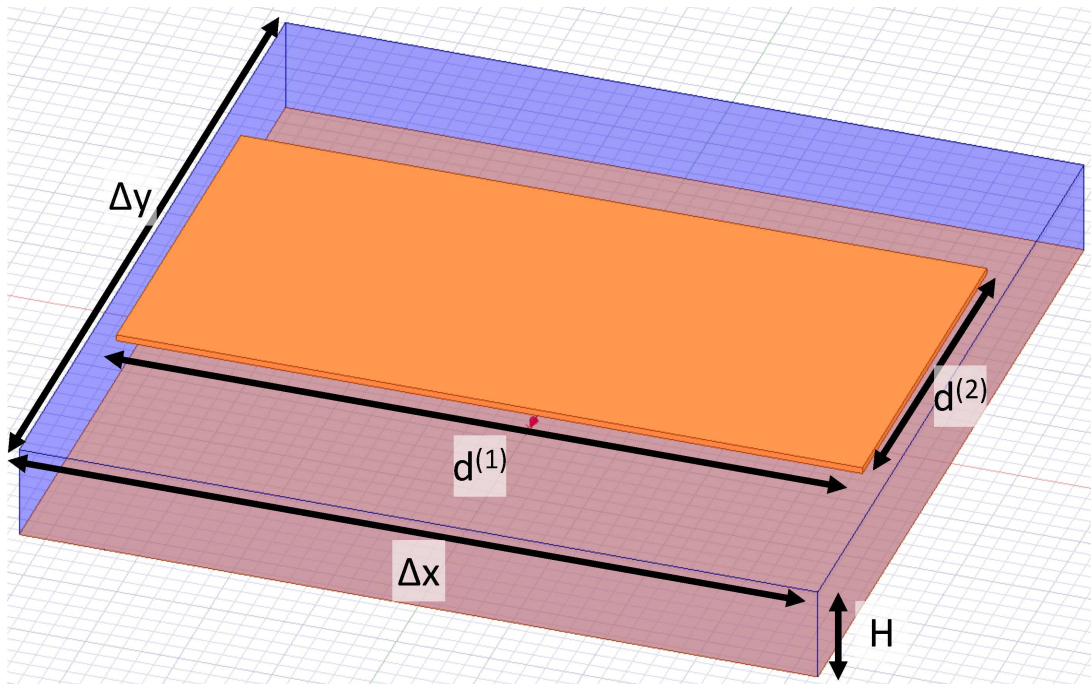
- **Figure 1.** *Problem Scenario* - Sketch of (a) the reference *SEME* and (b) the meta-atom geometry.
- **Figure 2.** *EMS Design Method* - Flowchart and building blocks.
- **Figure 3.** *Meta-Atom Analysis* ($\{\theta_{\psi}^{inc} = \varphi_{\psi}^{inc} = (0, 0) \text{ [deg]}; \psi \in \{TE, TM\}\}$, $L = 2$) - Behaviour of (a)(c) the magnitude and (b)(d) the phase of $\Gamma_{\psi}(\underline{d}, \mathbf{k}_{\psi}^{inc})$ versus the L descriptors of the meta-atom, $\{d^{(l)}; l = 1, \dots, L\}$: (a)(b) $\psi \rightarrow TE$ and (c)(d) $\psi \rightarrow TM$.
- **Figure 4.** *Numerical Validation* ($P \times Q = 20 \times 20$, $\theta_{\psi}^{inc} = \varphi_{\psi}^{inc} = \varphi_{\psi}^{refl} = 0 \text{ [deg]}$ ($\psi \in \{TE, TM\}$), $\theta_{TE}^{refl} = 30 \text{ [deg]}$, $\theta_{TM}^{refl} = -40 \text{ [deg]}$) - Sketch of the *HFSS* model of the synthesized *MP-SP-EMS*.
- **Figure 5.** *Numerical Validation* ($P \times Q = 20 \times 20$, $\theta_{\psi}^{inc} = \varphi_{\psi}^{inc} = \varphi_{\psi}^{refl} = 0 \text{ [deg]}$ ($\psi \in \{TE, TM\}$), $\theta_{TE}^{refl} = 30 \text{ [deg]}$, $\theta_{TM}^{refl} = -40 \text{ [deg]}$) - Plots of (a)(b) the phase of the ψ -th component of the local reflection coefficient, $\angle \Gamma_{\psi}(\mathbf{r}|\mathcal{D}, \mathbf{k}_{\psi}^{inc})$, in the *EMS* aperture Ω , (c)(d) the magnitude of the ψ -th component of reflected field pattern, $|\mathbf{E}_{\psi}^{refl}(u, v)|$, in the visible range Θ ($\Theta \triangleq \{(u, v) | u^2 + v^2 = 1\}$): (a)(c) $\psi \rightarrow TE$ and (b)(d) $\psi \rightarrow TM$.
- **Figure 6.** *Numerical Validation* ($P \times Q = 20 \times 20$, $\theta_{\psi}^{inc} = \varphi_{\psi}^{inc} = \varphi_{\psi}^{refl} = 0 \text{ [deg]}$ ($\psi \in \{TE, TM\}$), $\theta_{TE}^{refl} = 30 \text{ [deg]}$, $\theta_{TM}^{refl} = -40 \text{ [deg]}$) - Plot of the magnitude of the $\{\psi$ -th ($\psi \in \{TE, TM\}\}$ components of the reflected field pattern, $\{|\mathbf{E}_{\psi}^{refl}(u, v)|$ ($\psi \in \{TE, TM\}\}$), in the $\varphi = 0 \text{ [deg]}$ plane.
- **Figure 7.** *Numerical Validation* ($P \times Q = 20 \times 20$, $\{\theta_{\psi}^{inc} = -30 \text{ [deg]}, \varphi_{\psi}^{inc} = \varphi_{\psi}^{refl} = 0 \text{ [deg]}; \psi \in \{TE, TM\}\}$, $\theta_{TE}^{refl} = 30 \text{ [deg]}$, $\theta_{TM}^{refl} = -40 \text{ [deg]}$) - Pictures of (a) the sketch of the *HFSS* model of the synthesized *MP-SP-EMS* and (b) the magnitude of the $\{\psi$ -th ($\psi \in \{TE, TM\}\}$ components of the reflected field pattern, $\{|\mathbf{E}_{\psi}^{refl}(u, v)|$ ($\psi \in \{TE, TM\}\}$), in the $\varphi = 0 \text{ [deg]}$ plane.
- **Figure 8.** *Numerical Validation* ($\{\theta_{\psi}^{inc} = -30 \text{ [deg]}, \varphi_{\psi}^{inc} = \varphi_{\psi}^{refl} = 0 \text{ [deg]}; \psi \in \{TE, TM\}\}$, $\theta_{TE}^{refl} = 30 \text{ [deg]}$, $\theta_{TM}^{refl} = -40 \text{ [deg]}$) - Sketches of the *HFSS* model of the

synthesized *MP-SP-EMS* with (a) $P \times Q = 30 \times 30$ and (a) $P \times Q = 40 \times 40$ meta-atoms.

- **Figure 9.** *Numerical Validation* ($\{\theta_{\psi}^{inc} = -30$ [deg], $\varphi_{\psi}^{inc} = \varphi_{\psi}^{refl} = 0$ [deg]; $\psi \in \{TE, TM\}\}$, $\theta_{TE}^{refl} = 30$ [deg], $\theta_{TM}^{refl} = -40$ [deg]) - Plots of the magnitude of the $\{\psi$ -th ($\psi \in \{TE, TM\}\}$ components of the reflected field pattern, $\left| \mathbf{E}_{\psi}^{refl}(u, v) \right|$ ($\psi \in \{TE, TM\}\}$), in the $\varphi = 0$ [deg] plane in correspondence with the synthesized *MP-SP-EMS* with (a) $P \times Q = 30 \times 30$ [Fig. 8(a)] and (a) $P \times Q = 40 \times 40$ [Fig. 8(b)] meta-atoms.
- **Figure 10.** *Experimental Validation* ($P \times Q = 40 \times 40$, $\theta_{TE}^{inc} = -30$ [deg], $\theta_{TM}^{inc} = 40$ [deg], $\theta_{TE}^{refl} = 20$ [deg], $\theta_{TM}^{refl} = -20$ [deg], $\{\varphi_{\psi}^{inc} = \varphi_{\psi}^{refl} = 0$ [deg]; $\psi \in \{TE, TM\}\}$) - Pictures of (a) the *EMS* prototype and (b) the detail of the *EMS* metallizations.
- **Figure 11.** *Experimental Validation* ($P \times Q = 40 \times 40$, $\theta_{TE}^{inc} = -30$ [deg], $\theta_{TM}^{inc} = 40$ [deg], $\theta_{TE}^{refl} = 20$ [deg], $\theta_{TM}^{refl} = -20$ [deg], $\{\varphi_{\psi}^{inc} = \varphi_{\psi}^{refl} = 0$ [deg]; $\psi \in \{TE, TM\}\}$) - Plot of the magnitude of the ψ -th component of reflected field pattern, $\left| \mathbf{E}_{\psi}^{refl}(u, v) \right|$, in the $\varphi = 0$ [deg] plane: (a) $\psi \rightarrow TE$ and (b) $\psi \rightarrow TM$.



(a)



(b)

Fig. 1 - G. Oliveri *et al.*, “Multi-Functional Polarization-Based Coverage Control through ...”

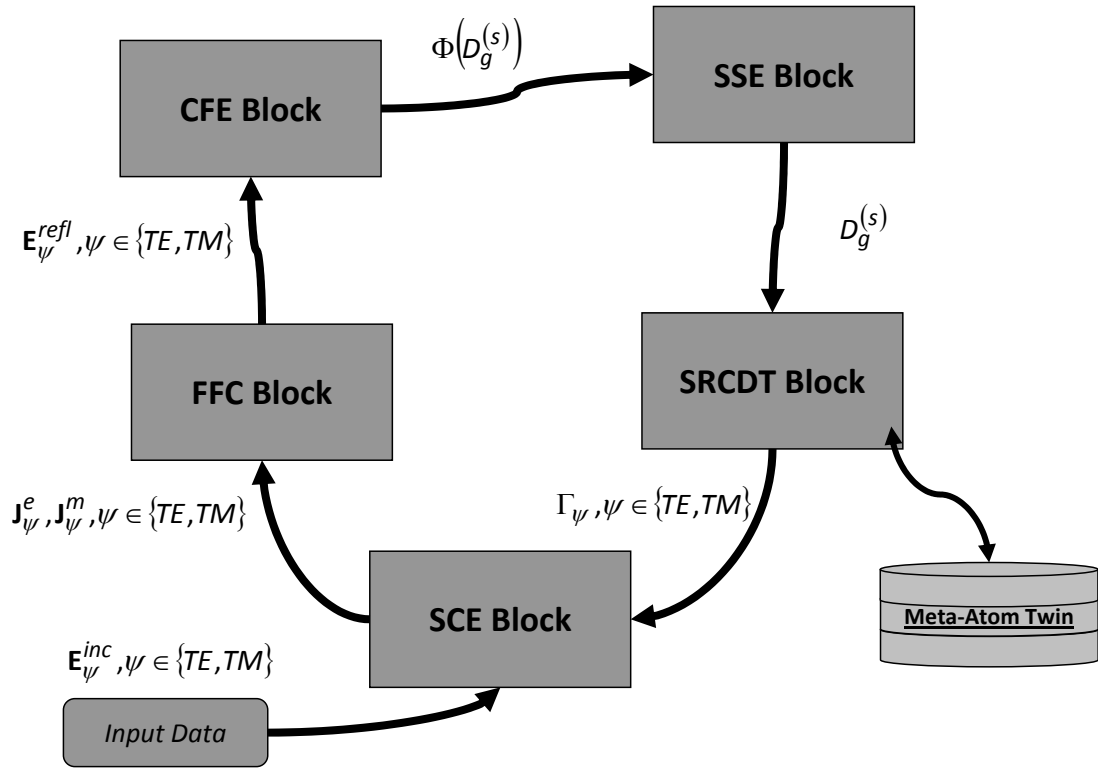


Fig. 2 - G. Oliveri *et al.*, “Multi-Functional Polarization-Based Coverage Control through ...”

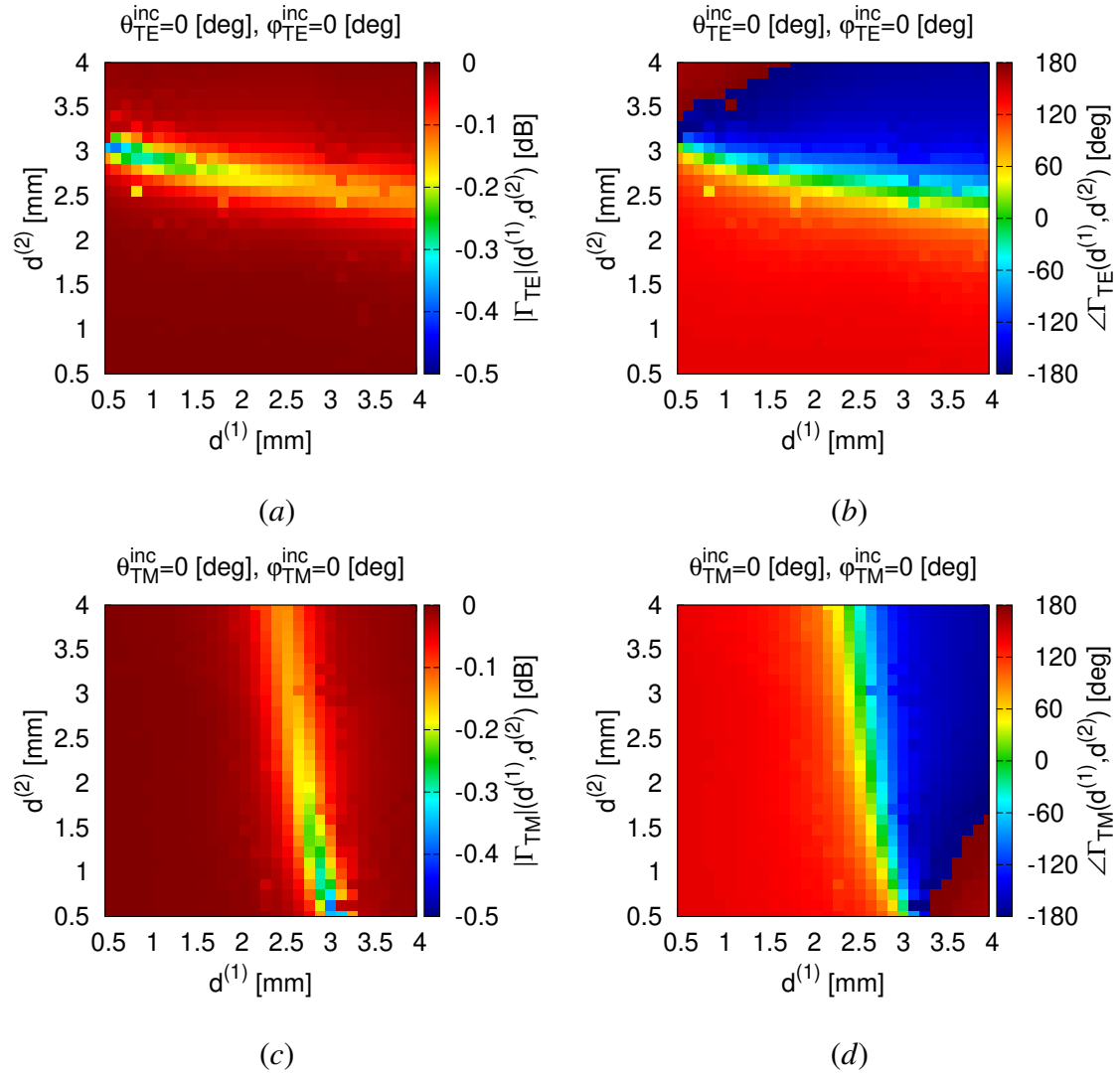


Fig. 3 - G. Oliveri *et al.*, “Multi-Functional Polarization-Based Coverage Control through ...”

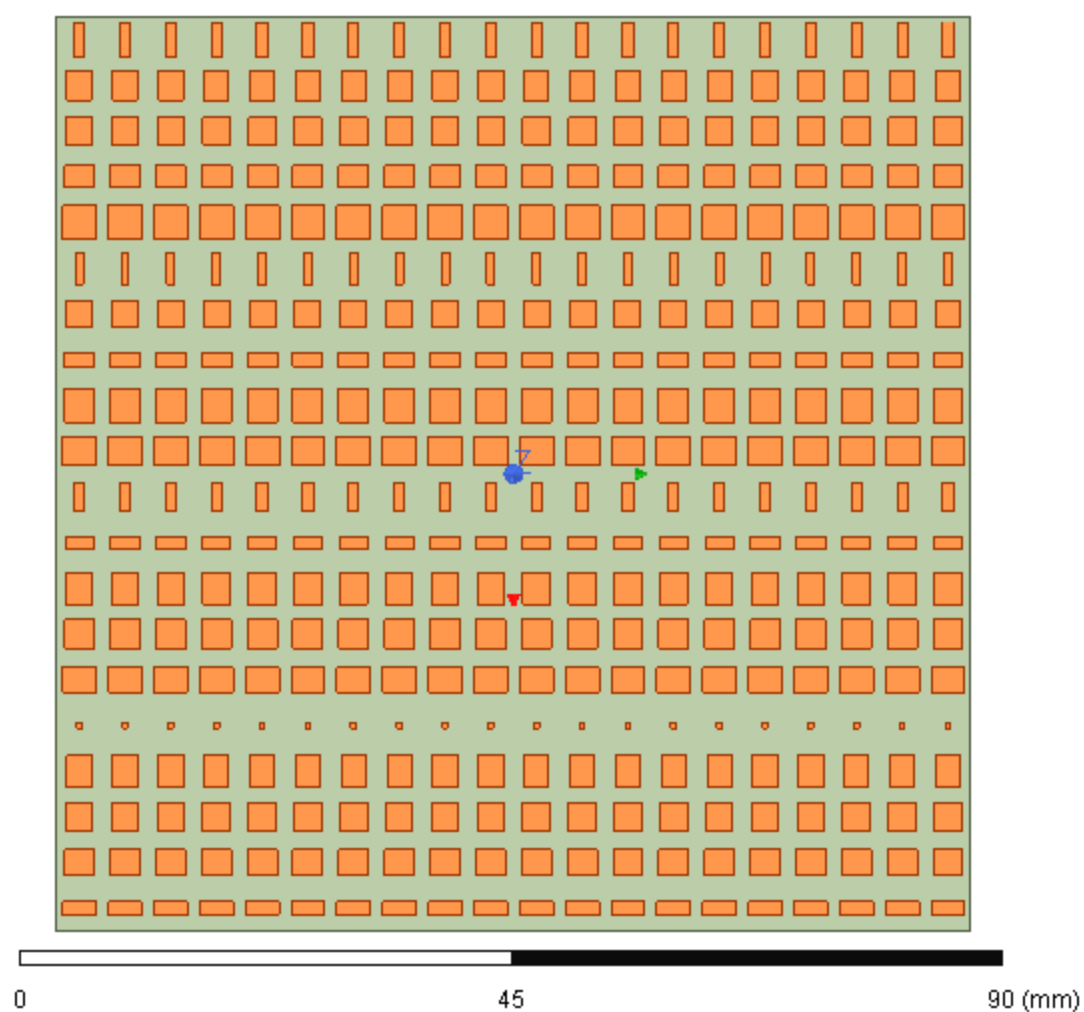


Fig. 4 - G. Oliveri *et al.*, “Multi-Functional Polarization-Based Coverage Control through ...”

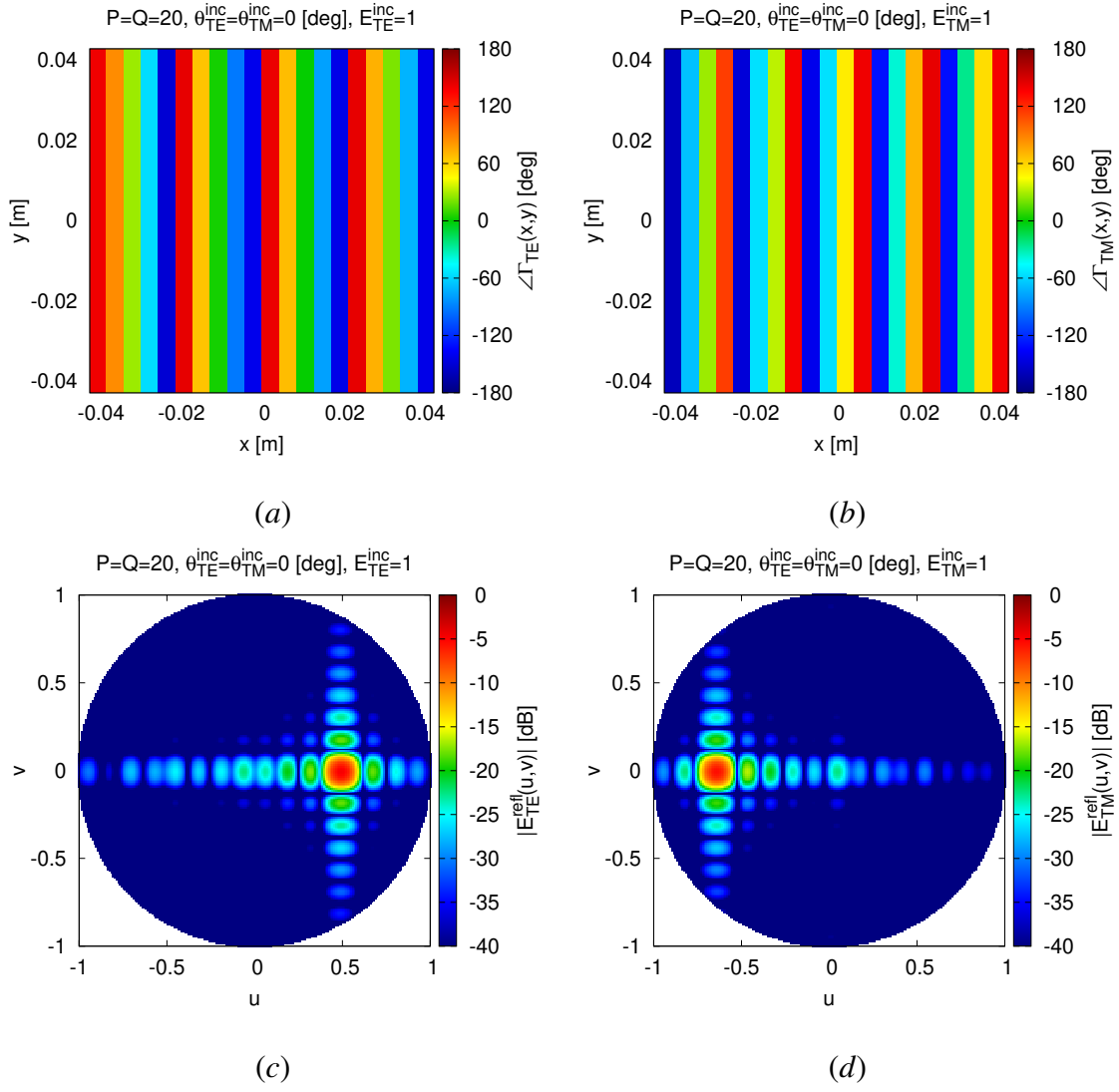


Fig. 5 - G. Oliveri *et al.*, “Multi-Functional Polarization-Based Coverage Control through ...”

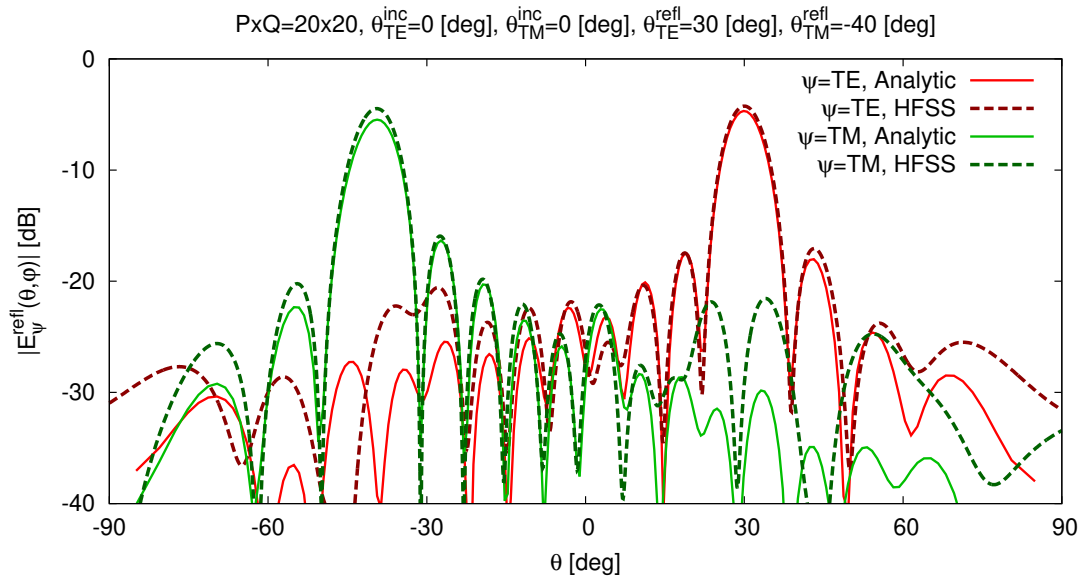


Fig. 6 - G. Oliveri *et al.*, “Multi-Functional Polarization-Based Coverage Control through ...”

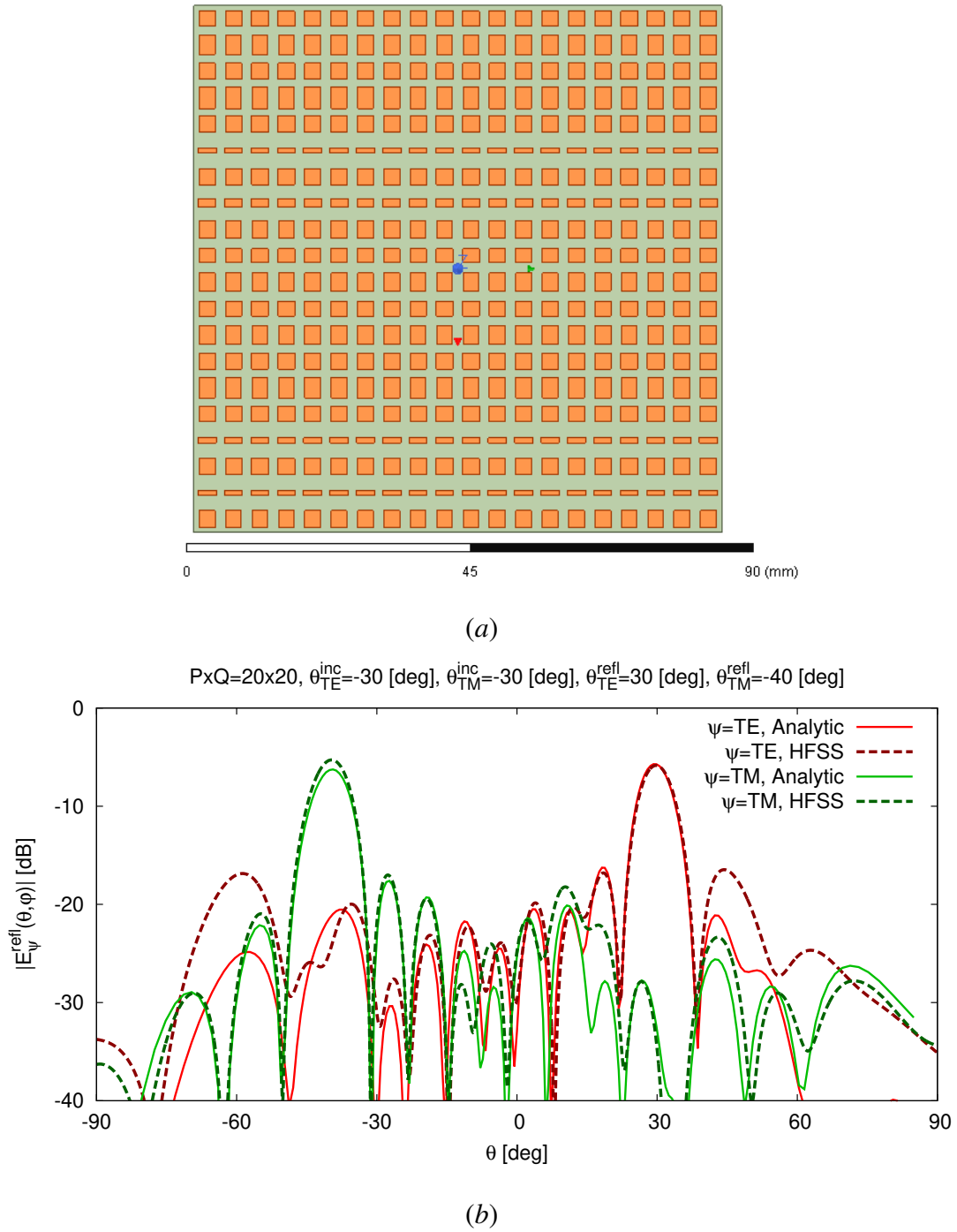
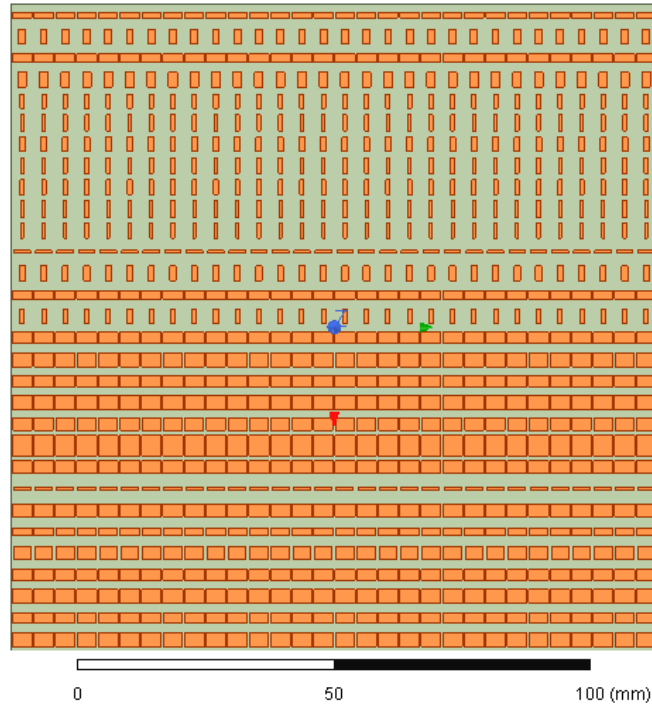
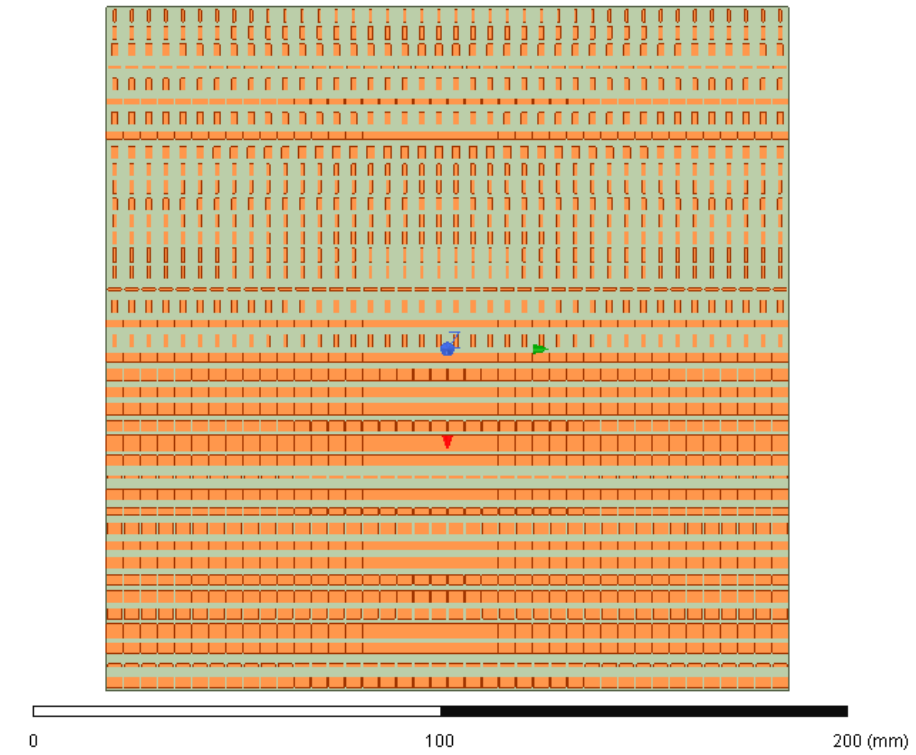


Fig. 7 - G. Oliveri *et al.*, “Multi-Functional Polarization-Based Coverage Control through ...”



(a)



(b)

Fig. 8 - G. Oliveri *et al.*, “Multi-Functional Polarization-Based Coverage Control through ...”

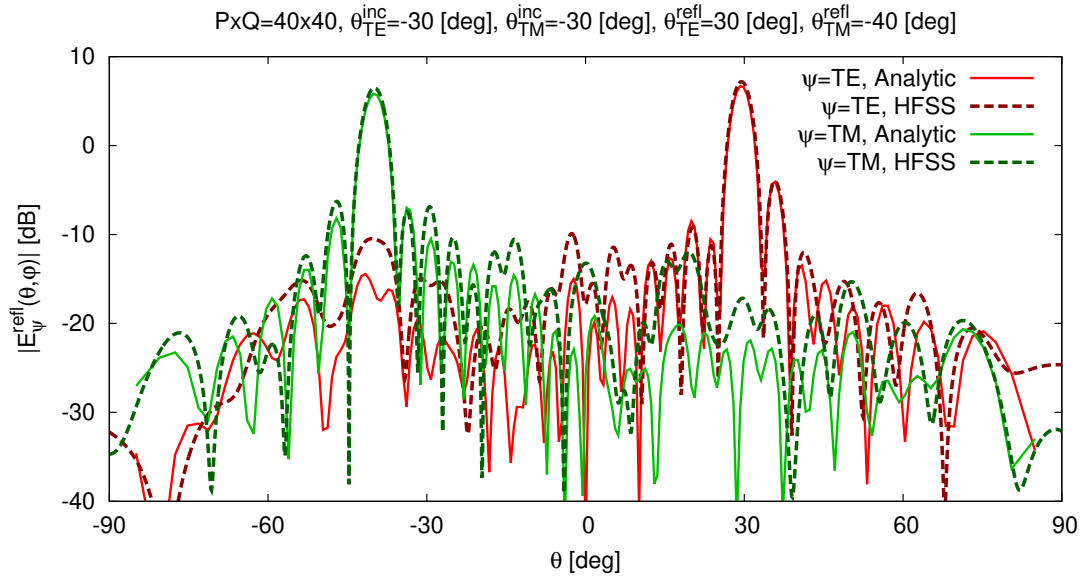
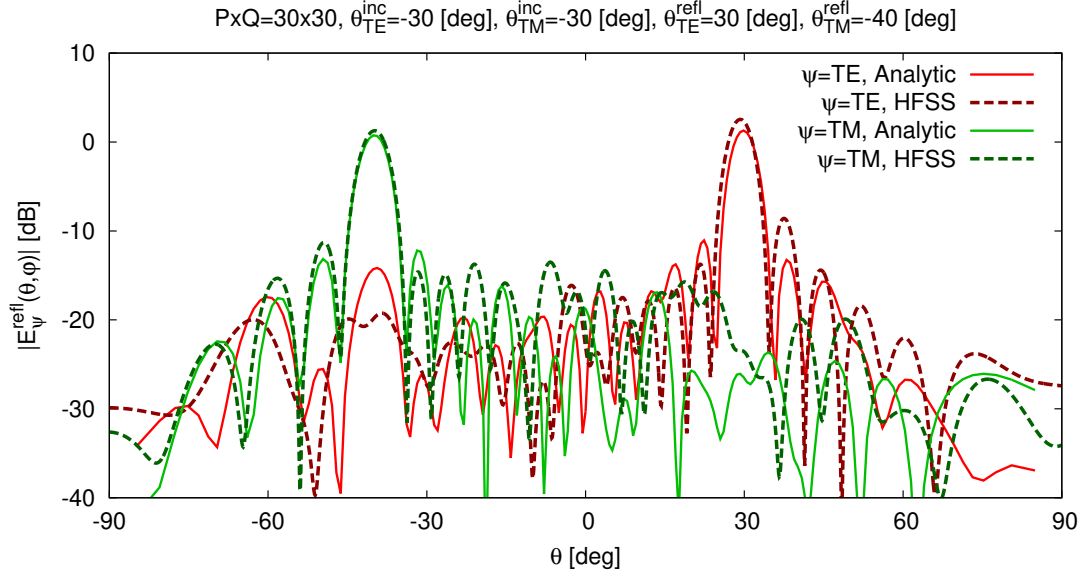
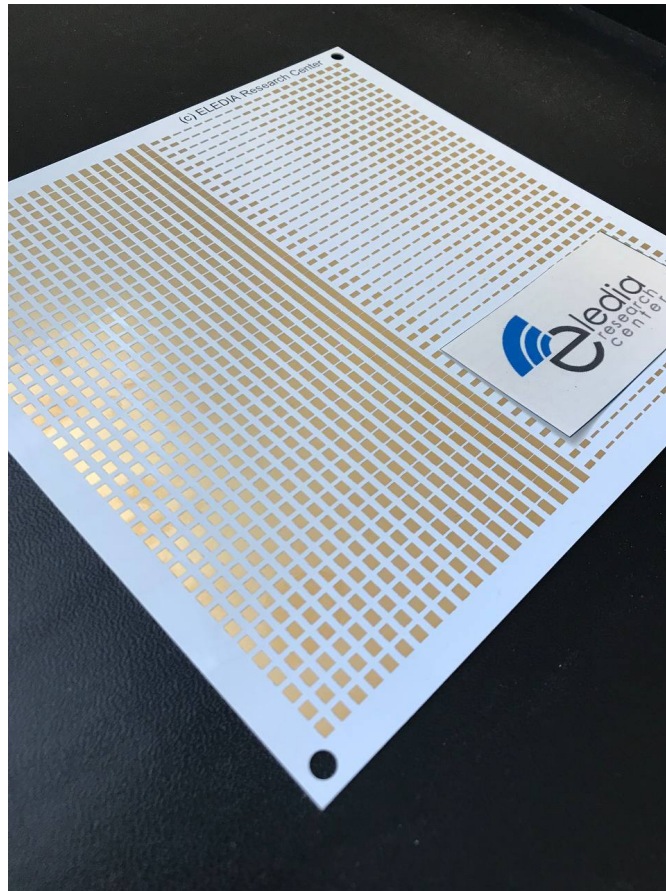
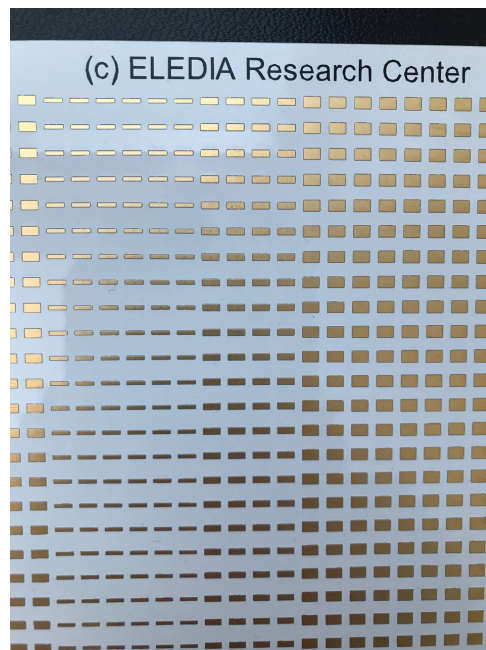


Fig. 9 - G. Oliveri *et al.*, “Multi-Functional Polarization-Based Coverage Control through ...”



(a)



(b)

Fig. 10 - G. Oliveri *et al.*, “Multi-Functional Polarization-Based Coverage Control through ...”

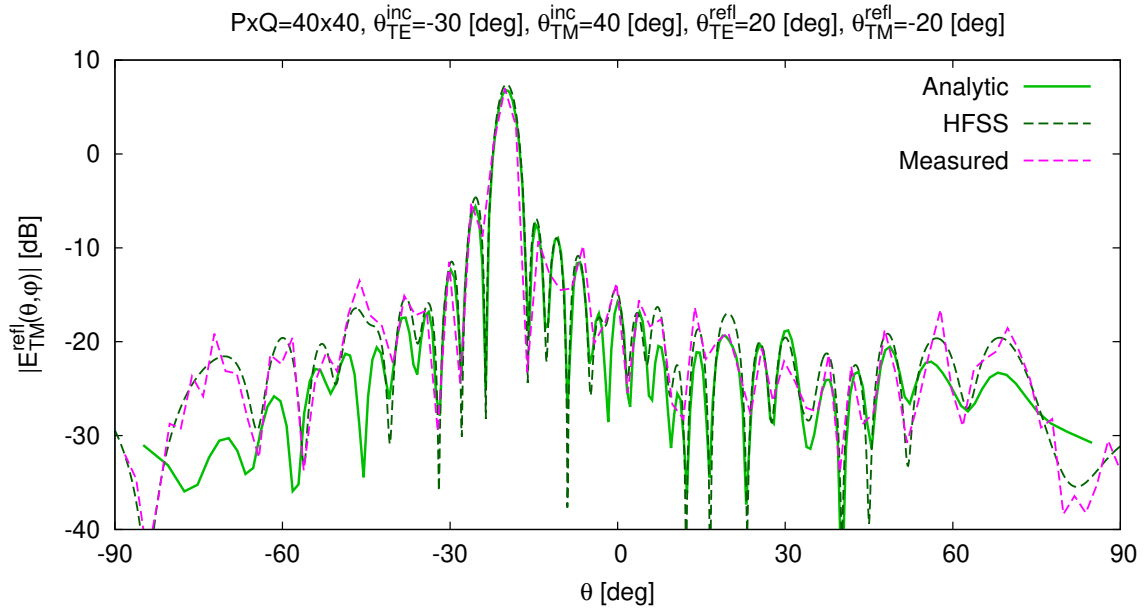
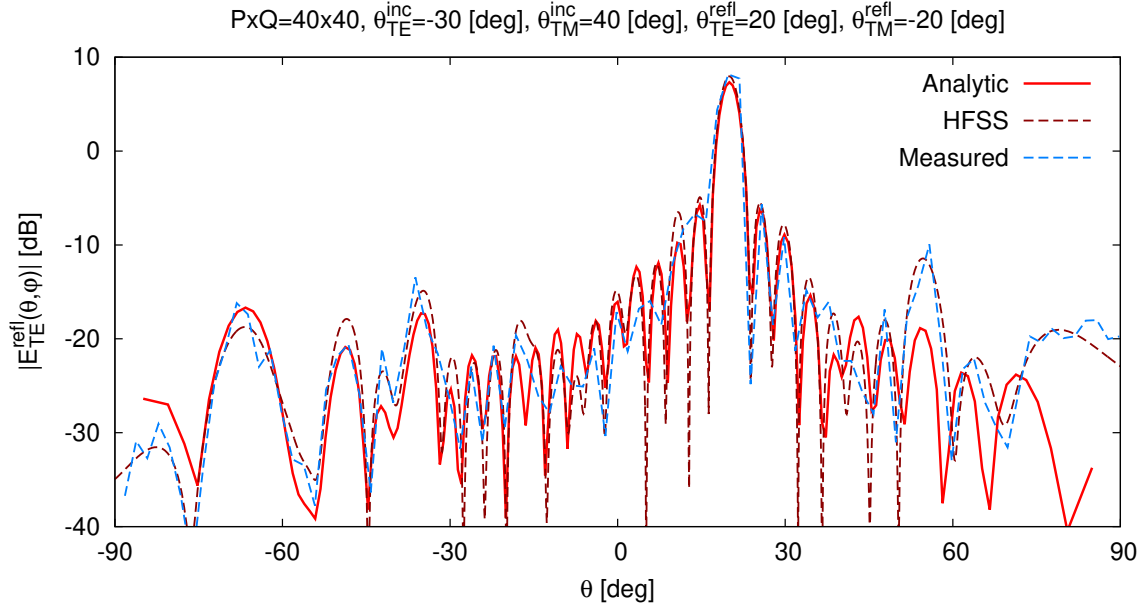


Fig. 11 - G. Oliveri *et al.*, “Multi-Functional Polarization-Based Coverage Control through ...”